



Cite this: *Soft Matter*, 2015,  
11, 4658

# Motility induced changes in viscosity of suspensions of swimming microbes in extensional flows†

Amarin G. McDonnell,<sup>a</sup> Tilvawala C. Gopesh,<sup>a</sup> Jennifer Lo,<sup>b</sup> Moira O'Bryan,<sup>b</sup>  
Leslie Y. Yeo,<sup>c</sup> James R. Friend‡<sup>c</sup> and Ranganathan Prabhakar\*<sup>a</sup>

Suspensions of motile cells are model systems for understanding the unique mechanical properties of living materials which often consist of ensembles of self-propelled particles. We present here a quantitative comparison of theory against experiment for the rheology of such suspensions in extensional flows. The influence of motility on viscosities of cell suspensions is studied using a novel acoustically-driven microfluidic capillary-breakup extensional rheometer. Motility increases the extensional viscosity of suspensions of algal pullers, but decreases it in the case of bacterial or sperm pushers. A recent model [Saintillan, *Phys. Rev. E: Stat., Nonlinear, Soft Matter Phys.*, 2010, **81**, 56307] for dilute active suspensions is extended to obtain predictions for higher concentrations, after independently obtaining parameters such as swimming speeds and diffusivities. We show that details of body and flagellar shape can significantly determine macroscale rheological behaviour.

Received 10th December 2014,  
Accepted 29th April 2015

DOI: 10.1039/c4sm02742f

www.rsc.org/softmatter

## 1 Introduction

Many living materials, such as suspensions of motile microbes or of ATP-powered cytoskeletal polymers, are large ensembles of nearly identical and motile subunits that interact strongly with their neighbours. Understanding the properties of such systems presents unique conceptual challenges. Since each elemental subunit such as a motile cell is by itself a driven-dissipative system, their collectives operate well out of equilibrium even in the absence of any external forcing. Local fluctuations in motion further have a non-thermal origin, and the fluctuation-dissipation theorem has been shown to be inapplicable in these systems.<sup>1</sup>

The recent development of a continuum framework that shows that these intrinsically non-equilibrium systems share universal features is therefore a significant theoretical breakthrough.<sup>2,3</sup> This theory of “active matter” suggests that a net average local alignment of self-propelled particles must, in a continuum description, lead to a contribution to the stress tensor arising from propulsive forces or “activity” of the particles. An interesting prediction is that particle activity must change

the macroscopic viscosity of the suspension. An axisymmetric self-propelled particle exerting a net propulsive thrust along its principal axis generates a hydrodynamic force dipole. The flow field around a single *E. coli* cell has been measured to be approximately that of a positive hydrodynamic dipole<sup>4</sup> which forces the ambient fluid around each particle axially outward towards its two ends. The suspension viscosity for such “pushers” is predicted to decrease below its value for a passive suspension of inactive particles of the same size, shape and concentration.<sup>5</sup> Conversely, a suspension of “pullers” with negative hydrodynamic dipoles will have a higher viscosity than a passive suspension. Quantitative microstructural models relating particle size, shape, concentration and motility to rheological properties are just beginning to emerge.<sup>6–9</sup>

These predictions are supported by experimental observations in shear flows with bacterial pushers<sup>10–12</sup> and algal pullers.<sup>13</sup> We present here the first measurements of *extensional* viscosities of suspensions of wild-type strains of the microalga *Dunaliella tertiolecta*, the bacterium *Escherichia coli* and mouse spermatozoa. *D. tertiolecta* uses its pair of flagella in a manner similar to the puller *Chlamydomonas reinhardtii* studied by Rafai *et al.*,<sup>13</sup> whereas *E. coli* and the sperm use flagellar tails to push forward, like *B. subtilis* studied by Sokolov and Aranson.<sup>10</sup> *E. coli* cells have multiple flagella and use run-and-tumble swimming by bundling and unbundling their flagella. Sperm were cultured under conditions to induce capacitation and hyperactive swimming.<sup>14</sup> Trajectories of cells swimming were analyzed to characterize their motility under quiescent conditions. Measurements of the extensional viscosity of live and dead cell suspensions were obtained with a novel microfluidic rheometer developed by

<sup>a</sup> Department of Mechanical and Aerospace Engineering, Monash University, Clayton, Australia. E-mail: prabhakar.ranganathan@monash.edu;  
Fax: +61 3 9905 1825; Tel: +61 3 9905 3480

<sup>b</sup> Department of Anatomy and Developmental Biology, Monash University, Clayton, Australia

<sup>c</sup> Micro/Nanophysics Research Laboratory, RMIT University, Melbourne, Australia

† Electronic supplementary information (ESI) available. See DOI: 10.1039/c4sm02742f

‡ Present address: Department of Mechanical Engineering, University of California-San Diego, San Diego, California, USA.

ref. 15. A recent model for dilute suspensions of self-propelled hydrodynamic dipoles<sup>7,8</sup> is extended here to the non-dilute regime to relate the non-Newtonian elongational viscosity of active suspensions to particle volume fraction. We compare predictions with this model against experimental data to demonstrate that despite the wide range of particle size, shape and motility characteristics, bulk mechanical behaviour of active suspensions may be accurately characterized in terms of a small number of parameters.

## 2 Experiments

### 2.1 Cell culture and suspensions

*D. tertiolecta* Butcher was collected and isolated from Port Phillip Bay, Victoria, in December 2009. Cultures were maintained at 20 °C in modified F-medium (30 g L<sup>-1</sup> aquarium salt, 250 mg L<sup>-1</sup> NaNO<sub>3</sub>, 18 mg L<sup>-1</sup> KH<sub>2</sub>PO<sub>4</sub>, 9 mg L<sup>-1</sup> iron(III) citrate (C<sub>6</sub>H<sub>5</sub>O<sub>7</sub>Fe), 9 mg L<sup>-1</sup> citric acid (C<sub>6</sub>H<sub>8</sub>O<sub>7</sub>), 0.2 mg L<sup>-1</sup> MnCl<sub>2</sub>·4H<sub>2</sub>O, 0.023 mg L<sup>-1</sup> ZnSO<sub>4</sub>·7H<sub>2</sub>O, 0.011 mg L<sup>-1</sup> CoCl<sub>2</sub>·6H<sub>2</sub>O, 0.005 mg L<sup>-1</sup> CuSO<sub>4</sub>·5H<sub>2</sub>O, 0.008 mg L<sup>-1</sup> Na<sub>2</sub>MoO<sub>4</sub>·2H<sub>2</sub>O, 0.65 µg L<sup>-1</sup> H<sub>2</sub>SeO<sub>3</sub> and traces of vitamin B12, biotin and thiamine<sup>16</sup>). 20 mL of inoculum were added to 400 mL of F-medium and incubated in 2 L glass bottles in a laboratory growth cabinet at 20 °C 0.1 °C with a 16 : 8 light dark cycle using white fluorescent lights with a photon flux of 60 µmol photons per m<sup>2</sup> per s. Cultures were bubbled with air through an aquarium air stone to provide a source of inorganic carbon (CO<sub>2</sub>). After 5 days, F-medium was added to bring the total culture volume to 1.5 L. Samples for experimentation were harvested after a further 6 days during the log-phase of growth into 50 mL polypropylene capped-tubes and centrifuged at 3500 rpm at 20 °C for 10 minutes to collect cell pellet.<sup>16</sup>

Wild-type *E. coli* K 12 strain was procured from ATCC, USA (#10798). Standard media in the form of Luria Bertini (LB) broth (#L3022, Sigma Aldrich; 10 g L<sup>-1</sup> tryptone, 5 g L<sup>-1</sup> yeast extract, 5 g L<sup>-1</sup> NaCl) and/or Luria Agar (#L2897, Sigma Aldrich) was used for bacterial culture. A UV-VIS spectrophotometer (#UV-2450, Shimadzu) was used to characterize the bacterial growth by measuring absorbance/optical density at 600 nm. About 0.5 mL of sterile LB broth was put into the sterile ATCC vial containing lyophilized culture. A small amount of the suspended culture (around 0.05 mL) was inoculated on to sterile Luria agar slants, and incubated at 37 °C for 18–20 hours. A single colony from an agar slant was transferred to 5 mL of sterile LB broth and incubated at 37 °C for 6–7 hours with vigorous shaking (at 170 rpm), till absorbance at 600 nm reached 0.4. About 0.3 mL of 50 wt% glycerol–water solution was added to 0.7 mL of this mid-log phase culture and stored at –73 °C for future use. From the glycerol-freeze stock, a tiny amount is scraped off and inoculated under aseptic conditions to 5 mL of sterile LB medium. The culture was incubated at 37 °C for 16–18 hours with vigorous shaking (at 170 rpm). A small amount (around 0.05 mL) was transferred into sterile LB media of 160 mL volume in a shake-flask. Cultures were incubated at 37 °C for 6–7 hours with vigorous shaking (at 170 rpm).

Sperm from C57BL (wild-type) mice, extracted from cauda epididymii using the back-flushing method<sup>17</sup> was added to 5 mL pre-warmed MT6 medium (125 mM NaCl, 2.7 mM KCl, 1 mM MgCl<sub>2</sub>·6H<sub>2</sub>O, 0.35 mM NaH<sub>2</sub>PO<sub>4</sub>·2H<sub>2</sub>O, 5.5 mM glucose, 25 mM NaHCO<sub>3</sub>, 1.7 mM CaCl<sub>2</sub>·2H<sub>2</sub>O, 60 µM bovine-serum albumin) containing methylcellulose and incubated at 37 °C for 90 min.

Algal cultures were centrifuged at 3500 rpm for 8 min at 20 °C and pellets were re-suspended in growth medium at desired concentrations. Lugol's iodine (100 g L<sup>-1</sup> KI, 50 g L<sup>-1</sup> iodine crystals) was added to Eppendorf tubes to kill algal cells. These were centrifuged, the supernatant removed and re-suspended in growth medium again. *E. coli* cultures after log-phase growth were centrifuged at 4550 rpm for 10 min at 4 °C, and pellets were re-suspended after weighing in a (pH 8.2) buffer of 10 mM K<sub>2</sub>HPO<sub>4</sub>, 0.1 mM EDTA and 0.2 wt% glucose to prepare suspensions of various cell volume fractions. Suspensions were exposed to UV light for 30–60 min to kill cells without significant lysis. Fresh sperm samples prepared as above were first tested in capillary-thinning experiments. Standing sperm suspensions for 90 min inactivated motility.

### 2.2 Particle tracking

Image-analysis was used to determine the average fractional area covered by cells at the focal plane; this was assumed to be equal to the volume fraction. In bacteria and algae, flagellar filaments were not resolved in the image analysis, and do not contribute to the volume fraction. Sample droplets were placed on Teflon-coated glass slides, with a coverslip on top. The gap width between slide and coverslip was typically 1 mm. Microscope videos for bacteria and algae were captured with 20× and 100× (Olympus) lenses, respectively, and a high-speed camera (SA5, Photron; 50 fps; 768 × 816 pixels). Swimming speeds and diffusivities were determined by processing images (ImageJ) and cell tracking (Imaris). Sperm suspensions were loaded onto both chambers on a 2×-Cel 80 µm slides chambers covered with 2×-Cel Cover Glass (Hamilton Thorne Research). Slides were inserted into a Hamilton Throne IVOS for computer-aided semen analysis (CASA). At least 1000 sperm were counted in each chamber. Sperm motility characteristics were analyzed through image analysis as done for the algae and bacteria. Sperm flagella were much thicker and were accounted for in the volume calculation.

### 2.3 Acoustically-driven microfluidic extensional rheometry

Unlike shear rheometry, techniques for reliable measurement of fluid properties in extensional flows have been established only relatively recently.<sup>18</sup> In capillary-breakup extensional rheometry (CaBER), a liquid bridge is usually first created by rapidly moving apart end-plates between which a sample drop is sandwiched. If the end-plate separation is large enough, the bridge subsequently begins to thin due to the Rayleigh–Plateau instability. The rate at which a liquid bridge thins is governed largely by the balance of the capillary stress against the inertial and viscous stresses induced by the extensional flow about the necking plane and hence it is in principle possible to extract the viscosity by monitoring the neck radius as a function of time.<sup>19</sup>

This technique has in the past been used for highly viscous samples.<sup>20</sup> Obtaining reliable measurements with low-viscosity complex fluids such as aqueous cell suspensions however presents two challenges. Firstly, mechanical motion of end-plates sets off inertial instabilities that quickly break up liquid bridges.<sup>18</sup> The motion within the liquid bridge following the sudden stopping of the end-plates is complex and is not described by a simple stress balance. Secondly, CaBER and other techniques based on capillary thinning of filaments are well established for viscoelastic fluids such as polymer solutions where liquid bridges thin exponentially in time, creating long-lived, slender and almost cylindrical filaments.<sup>21</sup> This permits the use of a simple stress-balance equation to extract the viscoelastic fluid stress at the necking plane from just a measurement of the radius  $R$  as a function of time  $t$ . For fluids with little or no elasticity, directly calculating the viscosity through the stress-balance has thus far been shown to be practicable again only for very viscous fluids where a cylindrical filament can form towards the final stages of breakup.<sup>20</sup> Thin cylindrical filaments do form close to break-up, but imaging these require the combination of ultra-fast and very high resolution photography.<sup>22</sup>

Several novel modifications to the original CaBER have been proposed to address the first of these issues. End-plates are moved at sufficiently high speeds in the Cambridge Trimaster device to overcome initial inertial instabilities.<sup>23,24</sup> In the slow-retraction-method, a low-viscosity liquid-bridge is first stabilized at an aspect-ratio smaller than that required to initiate capillary thinning, and then the end plates are moved apart slowly to initiate thinning in a controlled manner.<sup>25</sup> Microfluidic devices exploiting capillary thinning and breakup of a microjet ejected into an annular flow of another outer fluid have also been proposed.<sup>26</sup> Other forces have also been used in microfluidic devices to trigger capillary thinning in initially stable liquid bridges.<sup>27</sup>

Here, we use a method developed by Bhattacharjee *et al.*,<sup>15</sup> wherein the liquid-bridge is created and stabilized against capillary forces initially by power input from surface acoustic radiation (Fig. 1). In our experiments, a 20 MHz waveform generator (33220A, Agilent) was used to generate a surface acoustic wave (SAW) burst triggered by a second signal generator (WF1966, NF Corporation). The latter delivered a sinusoidal signal to an RF power amplifier (411LA, ENI), providing a fixed frequency and amplitude signal near the 36.7 MHz resonance frequency of the SAW substrate. An arrangement of curved inter-digitated transducers (IDTs) bonded to a piezoelectric substrate<sup>15</sup> focussed Rayleigh waves towards the point where a sessile droplet (1  $\mu$ l; approximately 1 mm dia.) rests (Fig. 1(b)). Energy from the SAW leaks into the droplet causing recirculation and bulk motion, leading to an elongated liquid that bridges a gap to an opposing parallel surface located 1.5 mm away from the SAW substrate. The opposing surface was coated with Teflon and was partially fouled to ensure that the jet adheres to the surface but does not spread. The SAW burst was ended after 1.5 ms which was found to be sufficient to create stable liquid bridges in all our samples. The liquid bridge then thins under the action of capillary forces, generating an extensional flow at the necking plane (Fig. 1(c)). The motion of the

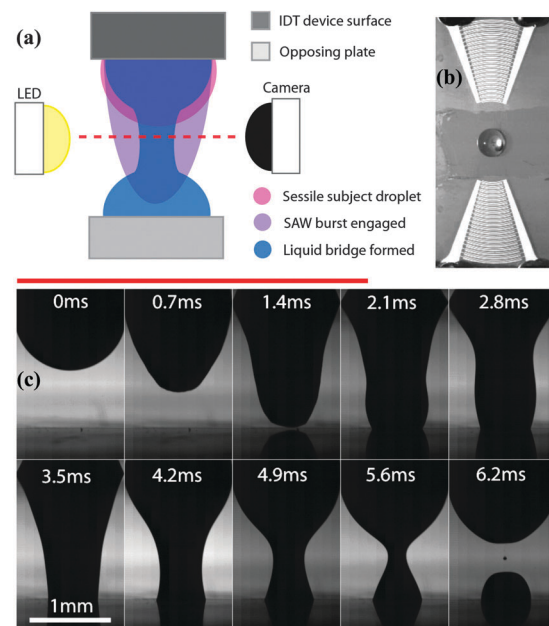


Fig. 1 (a) Schematic of experimental setup. (b) Curved inter-digitated transducers for focussing SAW into a sessile droplet. (c) Time-lapse images of the formation of a liquid bridge after ejection of a jet due to actuation of a sessile drop by SAW; the red-line indicates duration of the SAW pulse.

entire liquid bridge was captured using a high-speed camera (Photron SA5; 62 000 fps; image size: 1.35 mm  $\times$  2.14 mm (192  $\times$  304 pixels)) with a long-distance video microscope attachment (K2/SC, Infinity). The set-up is lit by a single LED lamp placed behind the filament. The radius of the neck in each image frame was obtained using standard image-analysis techniques. Initial transients were discarded in each case until the neck attained a diameter of 50 pixels ( $0.352 \pm 0.007$  mm); this was taken as the initial time ( $t = 0$ ) for all samples.

We avoid problems with imaging thin cylindrical filaments close to break-up altogether by using neck radius data during the early stages of the thinning while the axial curvature is still large. This is furthermore advantageous when handling particle suspensions since the effect of particle interactions with the air-liquid interface on the overall dynamics at the neck is weaker when the neck radius is large compared to particle dimensions. Rescaling the governing equations for slender but non-cylindrical Newtonian liquid-bridges<sup>28</sup> with the mid-filament radius  $R_0$  at  $t = 0$  (as defined above) and the Rayleigh time-scale,

$$\tau_R \equiv \sqrt{\frac{\rho R_0^3}{\gamma}}, \quad (1)$$

the decay of the rescaled neck radius  $R^* = R/R_0$  with rescaled time  $t^* = t/\tau_R$  is parametrized by the dimensionless volume and aspect ratio of the liquid bridge, and the Ohnesorge and Bond numbers, defined conventionally as

$$\text{Oh} \equiv \frac{\bar{\eta}}{3\sqrt{\rho\gamma R_0}}; \quad \text{Bo} \equiv \frac{g\rho R_0^2}{\gamma}, \quad (2)$$

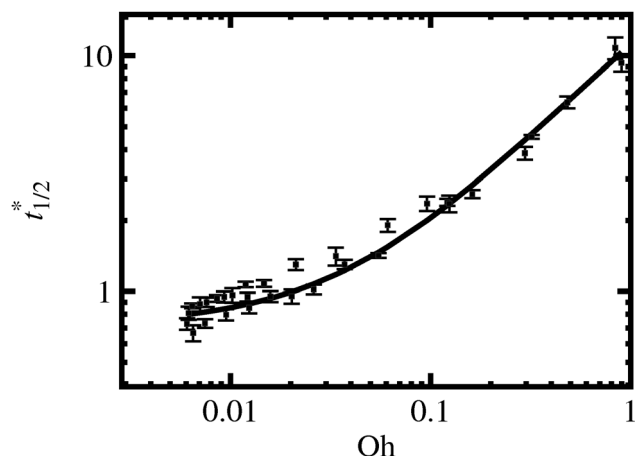


Fig. 2 Variation of liquid-bridge half-times with Oh: the curve is a linear least-squares fit of eqn (3) through the data.

where,  $\rho$ ,  $\gamma$  and  $\bar{\eta}$  are the density, surface tension coefficient and extensional viscosity respectively of a fluid sample and  $g$  is the gravitational acceleration. In our experiments, droplet volumes,  $R_0$  and the separation between bridge surfaces were kept constant. The Ohnesorge number for our samples varied by almost three orders of magnitude, whereas the variation in Bo was relatively much smaller (around 33%). Therefore, the Bond number can be assumed to be relatively constant. Under such conditions, the rescaled time  $t_{1/2}^*$  taken for the filament to neck to half its initial radius (*i.e.* the time to  $R^* = 1/2$ ) is predominantly governed by Oh.

Fig. 2 shows half-time data obtained for a range of Newtonian glycerol–water and sucrose–water mixtures whose properties ( $\eta = 3\bar{\eta}$ ,  $\gamma$  and  $\rho$ ) were independently measured. Surface tension of suspensions were measured using a tensiometer (Analite; Selby Scientific). Shear viscosities were measured with a Haake Mars (Thermo Scientific) shear rheometer. The form of the regression curve through the data in Fig. 2 is inspired by the asymptotic behaviour expected in the limits of vanishing or very large Oh. When  $Oh \rightarrow 0$ , inertia dominates and capillary thinning is insensitive to viscosity, whereas when viscous stresses dominate at high Oh, the breakup-time increases linearly with viscosity and Oh. We therefore fit a rational function of the following form through the experimental data:

$$t_{1/2}^* = \frac{K_0 + K_1 Oh + K_2 Oh^2}{1 + Oh} \quad (3)$$

The values of the coefficients for generating the empirical fit through the data as shown in Fig. S2 are given in the ESI.†

For a given non-Newtonian test sample that does not exhibit significant strain-hardening, the capillary breakup half-time is first extracted and normalized. The inverse of the rational function above in eqn (3) is then used to back out the Oh from observed  $t_{1/2}^*$ . From the definition of Oh in eqn (2), the extensional viscosity of the sample is obtained as  $\bar{\eta} = 3Oh\sqrt{\rho\gamma R_0}$ . The pre-factor of 3 is a consequence of the convention used to define Oh; no assumption is made here about a relationship between the extensional and shear viscosities of the sample.

We further note that as  $Oh \rightarrow 0$ ,  $R$ -vs.- $t$  data become insensitive to Oh. This is reflected in the levelling-off of the  $t_{1/2}^*$  data in Fig. 2 to a constant value at small Oh. Therefore, the method presented here becomes unreliable at very low values of Oh, since small errors in  $t_{1/2}^*$  imply large errors in Oh. In our experiments, the trend in  $t_{1/2}^*$  when Oh 0.01 is sufficient to allow us to back out Oh from measured half-times such that the error in the Oh backed out due to the noise in the calibration data in Fig. 2 is smaller than that due to the measurement error in  $t_{1/2}$  of the test sample. Significant differences between suspensions and suspending media are observed in plots of the decay of filament radius with time,<sup>†</sup> and there is no difficulty extracting their viscosities.

## 3 Modeling

### 3.1 Rheology

We are interested in quantitatively comparing theoretical predictions with experimental measurements of extensional viscosity on active suspensions with the aim of extracting the strengths of the active hydrodynamic dipoles for each of the organisms studied here. As we shall show later, a nonlinear dependence on particle volume fraction is observed which indicates that the suspensions are not dilute. We therefore need an analytical expression for the extensional viscosity of an active suspension as a function of the active dipole strength, particle concentration and other parameters such as the extensional strain-rate. Theoretical predictions are available in shear flows for non-dilute active suspensions,<sup>8,29</sup> but in extensional flows, only dilute suspensions have been analyzed so far.<sup>6,7</sup> As a first step, we use the Krieger–Dougherty equation (KDE)<sup>30–32</sup> to extend those results to more concentrated suspensions. The advantages and limitations of this approach will be discussed later after comparing predictions with experimental data.

The KDE was originally suggested for suspensions of (passive) spherical particles to describe the strong growth of viscosity as the particle density approaches the close-packing limit.<sup>30</sup> It has since then been applied for suspensions of non-spherical particles<sup>33</sup> as well as soft particles.<sup>34</sup> The KDE makes the mean-field assumption that when a new particle is added into the free-volume of a suspension, all its interactions with other particles and solvent can be modeled by treating the rest of the suspension as a homogeneous effective medium of a higher viscosity than the original suspending fluid.<sup>31,32</sup> The relative incremental influence of this particle on the overall viscosity is however assumed to be independent of the particle concentration itself and thus equal to its value at infinite dilution, all other parameters such as the strain-rate held constant. In dilute suspension theory, this relative influence exerted by each particle is described in terms of the intrinsic viscosity ration, which in extensional flows is defined as  $[\bar{\eta}] = \lim_{\phi \rightarrow 0} (\bar{\eta} - 3\eta_s) / (3\eta_s\phi)$ , where  $\bar{\eta}$  is the extensional viscosity of the suspension,  $3\eta_s$  is the extension viscosity of the Newtonian suspending medium of shear viscosity  $\eta_s$ , and  $\phi = nv_p$  is the volume fraction of particles, each of volume  $v_p$  and at a number density  $n$ .



This argument leads to the following equation for the relative extensional viscosity of a non-dilute suspension:<sup>31</sup>

$$\bar{\eta}_{\text{rel}} = \frac{\bar{\eta}}{3\eta_s} = \left(1 - \frac{\phi}{\phi_m}\right)^{-[\bar{\eta}]\phi_m}, \quad (4)$$

where  $\phi_m$  is a maximum volume fraction at which the steady-state viscosity diverges.

The intrinsic viscosity  $[\bar{\eta}]$  encodes for the effect of all parameters other than the concentration on suspension viscosity. Recent studies by Haines *et al.*<sup>6</sup> and Saintillan<sup>7</sup> have modeled the statistics of an axisymmetric self-propelled particle that stochastically changes its swimming direction while moving in an externally imposed homogeneous extensional flow, to obtain expressions relating  $[\bar{\eta}]$  to motility characteristics and strain-rate. We use Saintillan's expression here since it is applicable across a broader range of strain-rates.

In Saintillan's model, swimming cylinders of length  $L_h$  and diameter  $d$  translate with a mean speed  $U$  and autonomously change direction in an apparently random manner which gives rise to a non-Brownian rotational diffusivity,  $D_r$ . Passive particles (*e.g.* dead cells) on the other hand only have a diffusivity  $D_{r,0}$  that is solely due to thermal fluctuations. For a dilute suspension undergoing a homogeneous extensional flow of strain-rate  $\dot{\epsilon}$ , Saintillan<sup>7</sup> showed that

$$[\bar{\eta}] = \tilde{\chi} \left[ \frac{1}{2} \left( M + \frac{1}{3} \right) + \frac{3}{\text{Pe}} \left( \tilde{\gamma} + \tilde{\sigma} - \frac{1}{\tilde{\beta}} \right) \left( M - \frac{1}{3} \right) \right], \quad (5)$$

where the Péclet number— $\text{Pe} \equiv \dot{\epsilon}/D_r$  (or  $\dot{\epsilon}/D_{r,0}$ )—quantifies the ability of the extensional flow to reorient a particle against random orientational changes. The function  $M$  is a weak monotonically-increasing function of  $\tilde{\beta}\text{Pe}$ , where  $\tilde{\beta}$  is a constant shape-factor in the coupling of particle rotation to the straining motion of the ambient flow.<sup>†35</sup> Besides  $\tilde{\beta}$  and  $\text{Pe}$ , the equation above contains three other dimensionless parameters— $\tilde{\chi}$ ,  $\tilde{\sigma}$  and  $\tilde{\gamma}$ —characterizing the dipole moments of the hydrodynamic forces exerted by the straining flow around each particle, the propulsive thrust and the torques exerted by thermal fluctuations. These dimensionless parameters need to be related to measurable particle characteristics.

Cells that swim with flagella have complex shapes that on average can be approximated as being axisymmetric. We assume that the average frictional characteristics a cell can be represented by an effective cylinder of hydrodynamic length  $L_h$ . This length cannot however be directly measured. Instead, we express it terms of a ratio  $\lambda = L_h/L$ , where  $L$  is the measurable sum of the lengths of the head and the tail when completely stretched out. Then, the dimensionless strength of the flow-induced dipole is<sup>7,36</sup>

$$\tilde{\chi} = \frac{\pi\lambda^3 L^3}{12\nu_p \ln(2\lambda L/d)}. \quad (6)$$

The propulsive thrust generated by the inertialess swimmer and the corresponding frictional resistance to swimming are equal and opposite to one another, but act at different locations on the axis. A scaling argument for the strength of this propulsive dipole leads to<sup>7</sup>

$$\tilde{\sigma} = \pm \frac{\alpha \ln(2\lambda L/d)U}{\lambda^3 L D_r}, \quad (7)$$

where  $\alpha > 0$  is an unknown geometry-dependent pre-factor in the scaling analysis. The dipole is positive for pullers and negative for pushers, while for passive particles,  $\tilde{\sigma}_0 = 0$ . Torques due to thermal fluctuations tend to relax the orientational distribution of particles to its isotropic equilibrium state; their relative strength in an active suspension is represented by

$$\tilde{\gamma} = \frac{6k_B T \ln(2\lambda L/d)}{\pi\eta_s \lambda^3 L^3 D_r}, \quad (8)$$

where  $k_B$  is the Boltzmann constant and  $T$  is the thermodynamic absolute temperature of the suspension. The fluctuation-dissipation theorem (FDT) is valid for passive particles, in which case the rotational diffusivity for slender rods is related to friction and

$$D_{r,0} = \frac{3k_B T \ln(2\lambda L/d)}{\pi\eta_s (\lambda L)^3}. \quad (9)$$

Substituting this in eqn (8) above leads to  $\tilde{\gamma}_0 = 2$  for dead cells. No such simple relation is currently available in active systems for which  $D_r$  needs to be explicitly measured to obtain  $\tilde{\gamma}$ .

The model above for  $[\bar{\eta}]$  requires, besides the solvent conditions  $k_B T$  and  $\eta_s$ , independent measurement of the following parameters: the average geometric characteristics of the swimmers,  $L$ ,  $d$ ,  $\nu_p$ ; their motility characteristics  $U$  and  $D_r$  (or  $D_{r,0}$  for dead cells); and the hydrodynamic ratios  $\lambda$  and  $\alpha$ . The constant  $\tilde{\beta}$  is taken to be unity, which is appropriate for slender particles of large aspect ratio.<sup>7,35</sup> Out of these, the solvent parameters are obtained by standard techniques and the particle size characteristics  $L$ ,  $d$  and  $\nu_p$  are obtained through microscopy. As noted above, the value of  $D_{r,0}$  is effectively set by invoking the FDT and using  $\tilde{\gamma}_0 = 2$ . We discuss below the estimation of the motility parameters,  $U$  and  $D_r$ . It is more difficult to directly determine the ratios  $\lambda$  and  $\alpha$ , which are therefore treated as free parameters to be obtained by comparing model predictions to experimental data for  $\bar{\eta}_{\text{rel}}$ . Keeping in mind their physical significance, we assess later if the values for  $\lambda$  and  $\alpha$  obtained thus are plausible.

### 3.2 Active diffusivity

In the absence of flow, the trajectory of an active particle swimming in with a speed  $U$  along its principal axis with random reorientations of that axis can be modeled by a pair of Langevin equations for its instantaneous position  $\mathbf{r}(t)$  and orientation. The rescaled mean-squared displacement for such a particle in two dimensions is<sup>37</sup>

$$\widetilde{\text{MSD}} = \frac{\langle (\mathbf{r}(t) - \mathbf{r}(0))^2 \rangle}{(U/D_r)^2} = 4\xi\tilde{t} + 2(\tilde{t} - 1 + e^{-\tilde{t}}), \quad (10)$$

where  $\tilde{t} = D_r t$  and  $\xi = D_t D_r / U^2$ . The rescaled translational diffusivity  $\xi$  controls the shape of the  $\widetilde{\text{MSD}}$ -versus- $\tilde{t}$  curves:

$$\widetilde{\text{MSD}} \approx \begin{cases} (4\xi + \tilde{t})\tilde{t}, & \text{if } \tilde{t} \ll 1 \\ (4\xi + 2)\tilde{t}, & \text{if } \tilde{t} \gg 1 \end{cases}. \quad (11)$$

If translational diffusion is dominant and  $\xi \gg 1$ , then  $\widetilde{\text{MSD}} \approx 4\xi\tilde{t}$  always. When  $0 < \xi < 1$  on the other hand, one observes

diffusive-ballistic-diffusive behaviour. At short times when  $\tilde{t} \ll 4\tilde{\xi}$ ,  $\widetilde{\text{MSD}} \approx 4\tilde{\xi}\tilde{t}$ . At long time scales too, the behaviour is diffusive and  $\widetilde{\text{MSD}} \approx (4\tilde{\xi} + 2)\tilde{t}$ . Therefore, if the effective long-time translational diffusivity  $D_{\text{eff}}$  is defined such that  $\text{MSD} = 4D_{\text{eff}}t$ , then  $D_{\text{eff}} = D_t + (U^2/2D_r)$ . When  $4\tilde{\xi} \ll \tilde{t} \lesssim 1$ , the motion is ballistic with  $\widetilde{\text{MSD}} \approx \tilde{t}^2$ . Values of  $D_r$ ,  $D_t$  and  $U$  can be obtained from shift-factors by shifting experimental MSD-versus- $t$  data to match one of the dimensionless theoretical curves on a log-log plot.

## 4 Results and discussion

Experimental MSD data was obtained using suspensions of very low volume fractions with cell number densities smaller than  $L^{-3}$ . We find that this data for all the three organisms resembled the  $\tilde{\xi} = 0$  curve, indicating that translational diffusivity during swimming has a negligible influence (Fig. 3). The values of swimming speed and diffusivity thus extracted are reported in Table 1. The value of  $D_r$  for algae is comparable to those

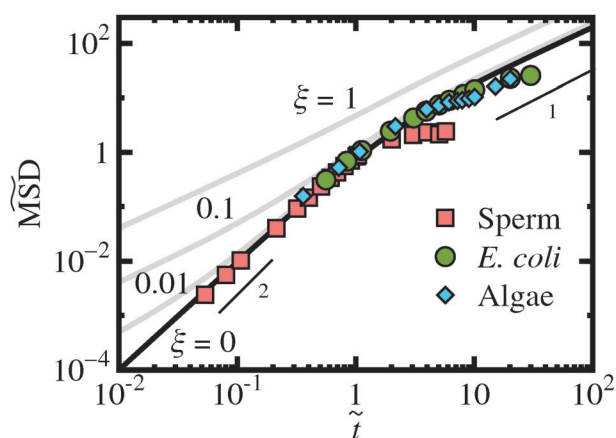


Fig. 3 Comparison of experimental data for the mean-squared displacement for algae, *E. coli* and mouse sperm with predictions for various values of the relative translational diffusivity  $\tilde{\xi}$ ;  $\widetilde{\text{MSD}} = \text{MSD}(D_r/U)^2$  and  $\tilde{t} = D_t t$ .

Table 1 Particle characteristics and model parameters

	Algae	Bacteria	Sperm
Geometric and motility characteristics			
$L$ ( $\mu\text{m}$ )	36	13	95
$d$ ( $\mu\text{m}$ )	2.8	1	3
$L/d$ ( $\mu\text{m}$ )	12.9	13	32
$U$ ( $\mu\text{m s}^{-1}$ )	30	5.5	31
$D_r$ ( $\text{s}^{-1}$ )	3	10	0.8
Free parameters			
$\alpha$	15	1	30
$\lambda$	0.6	0.3	0.7
$\phi_m$	0.7	0.7	0.7
Calculated parameters			
$\tilde{\chi}$	5.2	6.7	100
$\tilde{\gamma}$	$4.5 \times 10^{-3}$	$1.2 \times 10^{-2}$	$5.4 \times 10^{-5}$
$\tilde{\sigma}$	40	−2.7	−97
$F$ (pN)	46	0.6	260
$D_{r,0}$ ( $\text{s}^{-1}$ )	$6.8 \times 10^{-3}$	$6.1 \times 10^{-2}$	$2.2 \times 10^{-5}$

observed by Rafai *et al.*<sup>13</sup> in another blue-green algal species *C. reinhardtii*: they measured an average speed of  $U = 40 \mu\text{m s}^{-1}$ , and a long-time effective diffusivity of  $D_{\text{eff}} \approx 995 \mu\text{m}^2 \text{s}^{-1}$ , which corresponds to a rotational diffusivity of  $D_r \approx 0.8 \text{s}^{-1}$  assuming that the true translational diffusivity is negligible in that species as well. For *E. coli*, analysis of the 3D cell-tracking data suggests  $D_r \approx 3.5 \text{s}^{-1}$ ,<sup>38</sup> although a much lower value of  $D_r = 0.057 \text{s}^{-1}$  was reported by Drescher *et al.*<sup>4</sup> Some of this variability can be attributed to differences in strains and the media and protocols used for cell-tracking. In addition, there are also significant differences in the analyses of the run-and-tumble motion of *E. coli* cells to assign effective diffusivities. Although computer-aided analysis of sperm motility is well established in mammalian reproductive biology,<sup>39</sup> to our best knowledge, mean-square displacements have not been analyzed to determine effective diffusivities. The values of  $U$  extracted by fitting the theoretical prediction in eqn (10) through the mean-squared displacement data for the algae and bacteria are close to the values measured by direct observation (45 and  $4.7 \mu\text{m s}^{-1}$ , respectively). In the case of sperm however, the extracted value is significantly different from the direct measurement of an average speed  $70 \mu\text{m s}^{-1}$  for the motion of the sperm head which is comparable to average head speeds of around  $100\text{--}150 \mu\text{m s}^{-1}$  in hyperactive mice sperm.<sup>40,41</sup> This difference could be due to the fact that the sperm head oscillates about the mean trajectory of the cell.<sup>39</sup>

Fig. 4 presents the key results in our study. The top panel in the figure shows the evolution of the neck radius during capillary thinning for the highest volume fractions studied in each species; data at lower volume fractions is presented in the ESI.† We observe that capillary thinning of samples of live algal suspensions progresses more slowly than of samples of dead cell suspensions at the same volume fraction (top-panel, Fig. 4). The opposite behaviour is observed in bacterial and sperm suspensions. This is in line with the expectation that motility of pullers like *D. tertiolecta* tends to increase the viscosity whereas in pushers such as *E. coli* and sperm, viscosity decreases. The middle and bottom panels in Fig. 4 shows that the differences between the radius-versus-time data, and thus between the viscosities, of live and dead cell suspensions. These differences in *E. coli* are small but significant relative to experimental uncertainty. In comparison, the differences are larger in algae over a similar range of volume fractions. Data for sperm could only be obtained at low concentrations due to the small sample volumes collected from mice and limitations in concentrating them further. However, even at these low concentrations, the effect of motility on viscosity appears clear. The difference in viscosity between live and dead cell samples appears to increase with volume fraction for all three species.

To use the model to understand these trends, we first need to determine the strain rates in the experiments. As is well known, the instantaneous strain-rate  $\dot{\epsilon} = -2d \ln R/dt$  at the necking plane in CaBER experiments cannot be directly controlled but are determined by the liquid bridge dimensions and fluid properties. The radial decay in all our samples was observed to be approximately linear when  $t < t_{1/2}$ . The instantaneous strain-rate in this observation period for linear radial decay

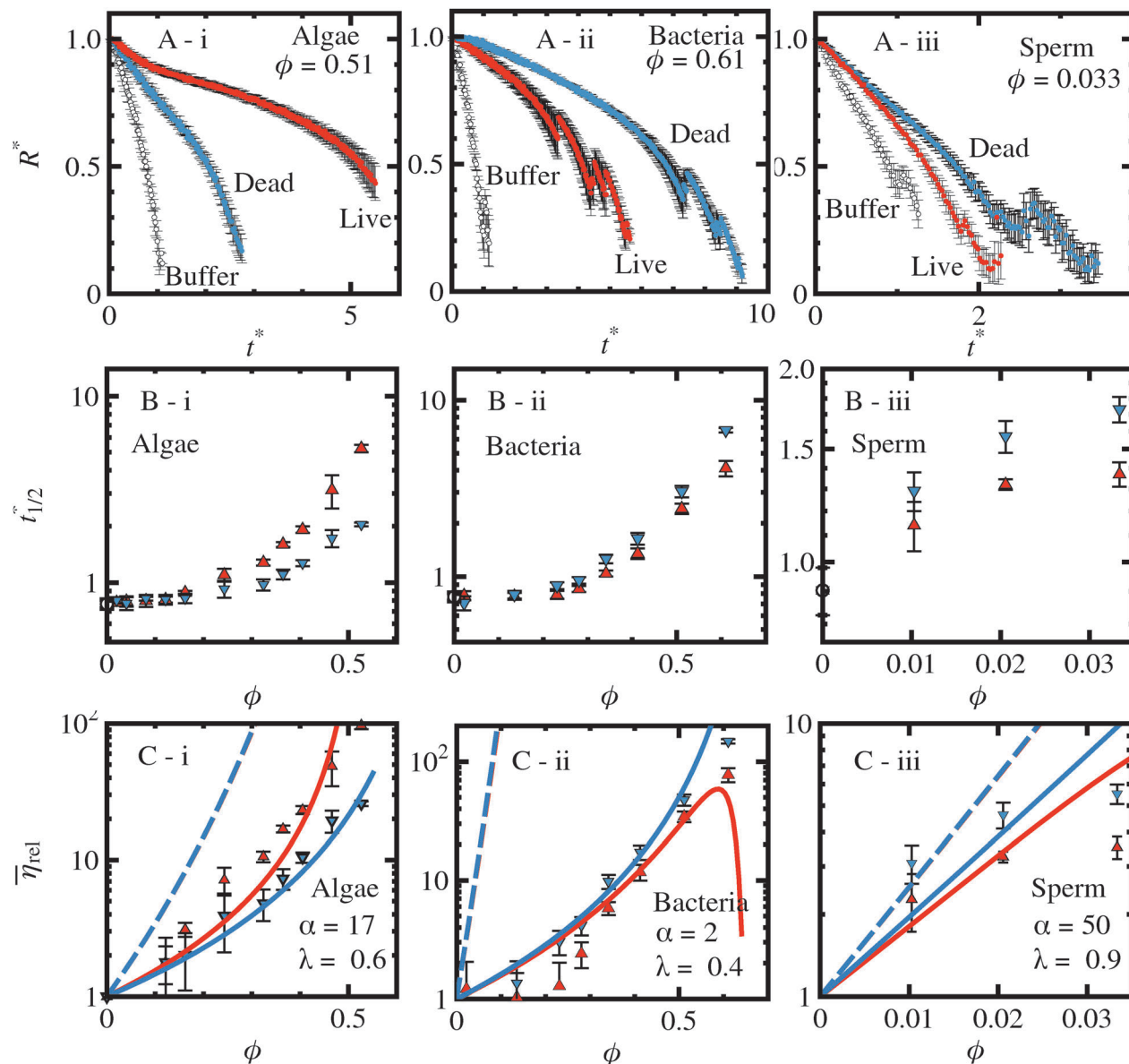


**Fig. 4** Top panel (A i–iii): radial decay observed during capillary thinning for the most concentrated algal, bacterial and sperm suspensions studied; middle panel (B i–iii): variation of dimensionless capillary thinning half-times with particle volume fraction; bottom panel (C i–iii): comparison of predictions of relative extensional viscosity  $\bar{\eta}_{rel} = \bar{\eta}/(3\eta_s)$  with experimental values extracted from measured  $t_{1/2}^* = t_{1/2}/\tau_R$ . In B and C, up- and down-triangles represent data for live and dead cell suspensions, respectively. Continuous curves in the bottom panel have been obtained with values of  $\alpha$  and  $\lambda$  as shown on the plots whereas dashed curves are predictions with both these parameters set to unity.

increases from  $1/t_{1/2}$  to  $2/t_{1/2}$ . We can thus estimate the average strain-rate from the observed  $t_{1/2}$  as  $\dot{\epsilon}_{avg} \approx \epsilon_{1/2}/t_{1/2} = 1.4/t_{1/2}$  since the Hencky strain at  $t_{1/2}$  for a linear radial decay can be shown to be  $\epsilon_{1/2} = 2 \ln 2$ . It is therefore clear from the systematic increase in  $t_{1/2}$  with concentration (Fig. 4B(i–iii)) that the average strain-rate  $\dot{\epsilon}_{avg}$  decreases with concentration as the increasing viscosity slows down capillary thinning. The strain-rate at any concentration in the range covered in the experiments was obtained using a cubic polynomial fit through the experimental  $\dot{\epsilon}_{avg}$ -vs.- $\phi$  data.<sup>†</sup> Values of  $\dot{\epsilon}_{avg}$  in our experiments ranged from about  $250 \text{ s}^{-1}$  at higher concentrations to  $2000 \text{ s}^{-1}$  for pure buffers.

Values of model parameters and other derived quantities for the three species are listed in Table 1. The ratio  $\lambda$  of the hydrodynamic length to the total end-to-end length  $L$  is a parameter that is estimated by visually bringing the predictions for dead cell suspensions into agreement with the experimental data. Since we are interested in order of magnitude estimates for this and the other free parameters  $\alpha$  and  $\phi_m$  in the model, a more rigorous least-squares fit was not pursued. The estimation of the parameter  $\lambda$  is not independent of the maximum packing fraction  $\phi_m$ . While  $\phi_m \approx 0.63$  is often used for spheres, there is no consensus on its value for anisotropic rod-like particles. It has been shown that  $\phi_m$  for such systems depends

on particle aspect ratio for dilute systems.<sup>32</sup> More concentrated suspensions of rod-like particles undergo an isotropic-to-nematic transition which is expected to occur at  $\phi \sim O((L/d)^{-1})$  at equilibrium.<sup>32,42</sup> The aspect ratios (based on the total end-to-end length; Table 1) of all three species are quite large. The concentrations of the algal and bacterial suspensions in our experiments are thus possibly well above the isotropic–nematic transitions for those systems. Although the volume fractions of the sperm suspensions are low, significant orientational effects due to interparticle interactions cannot be ruled out due to their large aspect ratios. A value of  $\phi_m = 0.7$  gives reasonable agreement of model prediction with dead cell data for all three species. With  $\lambda$  and  $\phi_m$  determined in this manner,  $\alpha$  is estimated to match predictions for live cells with experimental data for  $\bar{\eta}_{\text{rel}}$ .

How reasonable are the values in Table 1 of the key free parameters: the prefactor  $\alpha$  in eqn (7) for the active dipole, and the ratio  $\lambda$  of the hydrodynamic length to the total head–tail length of a swimmers? If both these parameters are set to unity, the values of the activity  $\bar{\sigma}$  are too low for all three species and predictions for live and dead cell suspensions are virtually indistinguishable, and these predictions are substantially different from the experimental data (dashed curves in Fig. 4C(i–iii)). The values of  $\lambda \lesssim O(1)$  required to obtain agreement with experiment appear reasonable given that flagella are never fully stretched out in swimming cells. Hydrodynamic interactions between the head and tail cause the parameter  $\alpha$  to be strongly geometry dependent. This can be seen by modeling a flagellar swimmer modeled as an asymmetric rigid dumbbell with Stokeslets of different hydrodynamic radii located at the head and tail respectively (Appendix A).<sup>43</sup> We obtain for such a dumbbell  $\alpha = 12[L_{\text{ht}}/L]^2/[(L_{\text{ht}}/a_h) - 3/2]$ , where  $L_{\text{ht}}$  is the distance between the head and tail centres and  $a_h$  is the hydrodynamic radius of the head. Although finite-size corrections can be expected to modify the singular behaviour when  $L_{\text{ht}}/a_h = 3/2$ , this result suggests that  $\alpha$  can vary over a wide range depending on the ratio  $L_{\text{ht}}$  and  $a_h$ . Viewed in this light, the variation in values of  $\alpha$  for the three very differently shaped cells appears plausible.

It is further possible to estimate propulsive forces (using the definition of  $\bar{\sigma}$  in eqn (7) and its values in Table 1) as  $F = \sigma/L_h$ . Bayly *et al.*<sup>44</sup> analyzed the flagellar stroke of a single *C. reinhardtii* using resistive force theory to estimate an average power dissipation of about 5 fW, which when combined with an average speed of around  $40 \mu\text{m s}^{-1}$  in that species,<sup>13</sup> yields  $F = 125$  pN. Drescher *et al.*<sup>4</sup> estimated a propulsive force of  $F = 0.43$  pN directly in a wild-type *E. coli* cell by measuring the flow field around it during a straight run. Schmitz *et al.*<sup>45</sup> used a microprobe to measure the force required to stall the motion of a bull sperm flagellum to be  $F = 250$  pN. These values from direct single cell or flagellum measurements are comparable to the values of  $F$  in Table 1.

The predictions of  $\bar{\eta}_{\text{rel}}$  in the bottom panel of Fig. 4 were generated using the KDE after first calculating the intrinsic viscosities  $[\eta]$  with eqn (5) for the ranges of Péclet numbers observed for live and dead cells. The Péclet numbers calculated as  $\text{Pe} = \dot{\epsilon}_{\text{avg}} D_r$  with the rotational diffusivities for live cells in Table 1 are plotted in Fig. 5(a). The Péclet number governs the

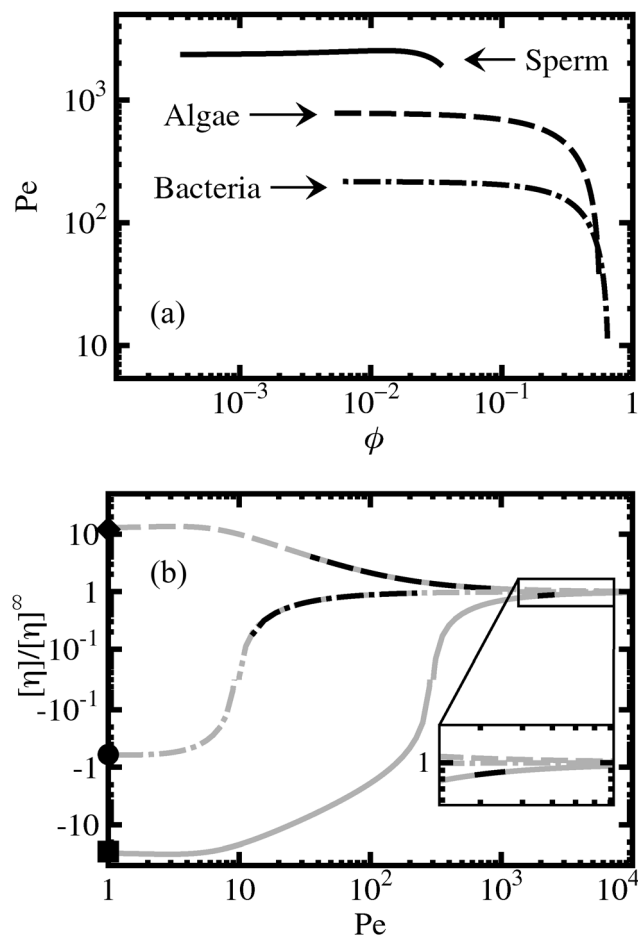


Fig. 5 (a) Experimentally observed variation of Pe with volume fraction in live samples; the curves have been obtained by polynomial regression of strain-rate data.<sup>†</sup> (b) Effect of flow strength on intrinsic viscosity of live cell suspensions of sperm (continuous), algae (dashed) and bacteria (dot-dashed curve): the black portions of the curves represent the experimentally observed Pe values in (a); the filled symbols on the co-ordinate axis represent the zero-Pe limit  $[\eta]^0/[\eta]^\infty$  obtained with the model parameters in Table 1.

competition between flow and diffusion and the values of  $\text{Pe} \gg 1$  in Fig. 5(a) indicate that the flow completely overcomes the tendency for diffusion to make the orientational distribution isotropic and that particles are aligned along the principal stretching axis of the uniaxial extensional flow. It is typically expected that at such high values of Pe, the flow-induced dipole will dominate to such an extent that no difference between live and dead cells suspensions should be observed. How does one then explain the clear differences observed between live and dead samples in Fig. 4?

To answer this question, we firstly note that the small rotational diffusivities (Table 1) of dead cells mean that their Péclet numbers are very large for all the three species and across the entire range of volume fractions studied. In fact, the values of  $[\eta]$  for dead cells are nearly identical to the value  $[\eta]^\infty = 2\tilde{\chi}/3$  in the limit  $\text{Pe} \rightarrow \infty$  purely due to the flow-induced dipole. The Péclet numbers of the live samples on the other hand, while still high, are much smaller than those of the dead samples at the same volume fraction. Fig. 5(b) plots as a function



of Pe the ratio of  $[\eta]$  for the live samples with the value of  $[\eta]^\infty$  for the dead cells of that species. The curves have been generated using the parameters in Table 1; the portions of the curves in the range of live-cell Pe in the experiments in Fig. 5(a) are shown in black in Fig. 5(b). The plots show that the magnitude of the parameter  $\tilde{\sigma}$  in an active suspension can be such that the contribution of propulsive dipole can still be relatively large even when  $Pe \gg 1$  and cells are highly aligned by the flow. Therefore,  $[\eta]/[\eta]^\infty$  is significantly different from unity and live and dead cell samples have clearly different viscosities even over the range of experimentally observed Pe values. Moreover, with increasing cell volume fraction, not only are there more cells per unit volume contributing propulsive stresses, the strain-rate and Pe numbers decrease (Fig. 5(a)) boosting the relative contribution of active dipole.

The effect of activity on  $\bar{\eta}_{rel}$  in Fig. 4 appears strongest in algae because of the combination of a large propulsive dipole and particle concentrations. The dipole is much weaker in *E. coli* pushers, leading to a smaller effect of activity, although they have the largest swimming diffusivity and lowest Pe values among the three species. In contrast,  $\tilde{\sigma}$  in sperm appears to be so large that their live suspensions show a clearly measurable effect of motility even at very low cell densities and despite very large Pe values.

Interestingly, in the bottom panel of Fig. 4, a maximum is predicted by the model for live *E. coli* suspensions. This is because the projected Pe at high concentrations decreases to low enough values at which  $[\eta]$  for *E. coli* falls rapidly (Fig. 5(b)). In fact, at even lower Pe values, the negative values of  $\tilde{\sigma}$  for the pushers *E. coli* and sperm are predicted to lead to negative  $[\eta]$  (Fig. 5(b)), which will result in live cell suspensions being less viscous than the suspending medium. This intriguing effect has been predicted previously in a number of theoretical studies.<sup>6–8,29</sup> Although such low strain-rates cannot be practically realized with extensional rheometers currently, they are accessible in shear rheometers. Gachelin *et al.*<sup>11</sup> recently reported this effect with *E. coli* suspensions in a microfluidic shear rheometer. Fig. 5(b) shows that the effect is likely to be much more dramatic at with sperm suspensions at low Pe: in extensional flows, the parameters we have obtained for sperm lead to a very large negative zero-Pe limit  $[\eta]^0 = \tilde{\gamma}(2/9 + \tilde{\beta}/15(\tilde{\gamma} + \tilde{\sigma} - 1/\tilde{\beta})) = -1.9 \times 10^3$ .

The model presented here is but a first step towards a more complete understanding of the role of concentration on the extensional rheology of active particle suspensions. The use of the KDE to model the effect of concentration has its limitations. It does not for instance directly take into account changes in particle motility in pusher suspensions brought about by the emergence of large-scale coherent structures and collective motion due to inter-particle hydrodynamic interactions.<sup>12,46,47</sup> However, although  $U$  and  $D_r$  in Saintillan's equations for  $[\eta]$  in principle describe the motility of isolated swimmers, it may be possible to use concentration-dependent average speeds and long-time diffusivities measured in non-dilute suspensions as particles execute collective motion.

Another limitation is that the KDE cannot predict non-monotonic concentration dependence when all other parameters including the strain-rate are held fixed. Ryan *et al.*<sup>29</sup>

used simulations of swimming hydrodynamic dipoles with short-range excluded-volume repulsion to show that the shear viscosity of pusher suspensions can display a minimum with respect to concentration at a fixed shear-rate. As pointed out earlier, if the active dipole  $\tilde{\sigma}$  is strongly negative, the intrinsic viscosity can be negative in pusher suspensions. In such a case, the viscosity decreases linearly with concentration in the dilute regime. The contribution to the viscosity due to pair-wise excluded-volume repulsions between particles on the other hand always increases more strongly with concentration. The initial decrease with concentration is thus followed by an increase at higher concentration with a minimum at a particular concentration. Such behaviour has been observed in experiments with *E. coli* by Gachelin *et al.*<sup>11</sup> Negative intrinsic viscosities nevertheless do not always occur in pushers, as shown in Fig. 5(b). In either shear or extensional flows, the intrinsic viscosity is positive above a critical strain-rate whose value depends on the effective rotational diffusivity and the magnitude of the active dipole.<sup>6,8</sup> For pullers, and obviously for passive suspensions or dead cells, the intrinsic viscosity is always positive. In all these cases, the KDE-based model provides a good semi-empirical description of the monotonic growth of viscosity with concentration.

## 5 Conclusions

Our experimental observations with a surface-acoustic-wave driven microfluidic rheometer indicate that particle motility has a clearly measurable influence on the rheology of suspensions. Capillary thinning of liquid bridges proceeded more slowly in suspensions of algal pullers than those of dead cells at the same volume fraction, whereas bacterial and sperm pushers tended to hasten thinning. The difference in the effective viscosity between suspensions of live and dead cells was found to systematically increase with concentration.

Predictions with a model that combined the Krieger–Dougherty equation for the relative viscosity of suspensions with an equation derived by Saintillan<sup>7</sup> for the intrinsic extensional viscosity of active suspensions were found to be in good qualitative agreement with the experimental observations. Our results show that the propulsive dipole even in weak swimmers such as *E. coli* can contribute significantly to fluid stresses even at high Péclet numbers when flow dominates over swimming noise. While parameters such as the properties of the suspending medium, the physical dimensions of the cells, and their swimming speeds and effective rotational diffusivities could be determined from independent measurements, model predictions appear to depend crucially on hydrodynamic details such as the effective hydrodynamic length of the swimmer and the contribution of hydrodynamic interactions between the head and tail to the propulsive dipole moment. Values of these parameters required to match predictions with experimental data lead to estimates for propulsive forces in the three species that are in line with data in literature on direct force measurements with single cells or flagella.

The principal advantages of using the Krieger–Dougherty equation to model the influence of particle concentration are its simplicity, and that it enables comparison of the rheological behaviour of different active or passive suspensions in terms of a few quantitative parameters. The agreement between predictions and experiments suggests that improved models for non-dilute active suspensions may be derived by combining more accurate alternatives of the Krieger–Dougherty equation for describing concentration effects with refinements of the dilute solution theory for active suspensions that account for the hydrodynamic characteristics of swimming particles and their propulsion. Such models open up the possibility of routinely and precisely extracting propulsive forces in motile cells by rheometry of active suspensions.

## A Self-propelled asymmetric dumbbells

A swimmer is modeled as a rigid asymmetric dumbbell with Stokeslets of hydrodynamic radii  $a_h$  and  $a_t$  located at the hydrodynamic centres of the head and tail respectively.<sup>43</sup> The rigid swimmer translates with a velocity  $\mathbf{u}$  relative to the unperturbed ambient fluid as a result of the actuation of the tail (Fig. 6). The tail generates a thrust of  $\mathbf{F}_p$ . The total hydrodynamic force on the tail is the sum of  $\mathbf{F}_p$  and its frictional resistance to the translational motion:

$$\mathbf{F}_t = -\zeta_t(\mathbf{u} + \boldsymbol{\Omega} \cdot \mathbf{F}_h) + \mathbf{F}_p, \quad (12)$$

where  $\zeta_t = 6\pi a_t \eta_s$  is the drag coefficient of the tail and  $\boldsymbol{\Omega}$  is the tensor describing the hydrodynamic interaction tensor between the head and tail such that the velocity perturbation at the tail due to the hydrodynamic force  $\mathbf{F}_h$  on the head is  $-\boldsymbol{\Omega} \cdot \mathbf{F}_h$ .<sup>48</sup> The head only experiences frictional resistance, and

$$\mathbf{F}_h = -\zeta_h(\mathbf{u} + \boldsymbol{\Omega} \cdot \mathbf{F}_t). \quad (13)$$

The total hydrodynamic force on the inertialess swimmer must be zero in the absence of external forces:

$$\mathbf{F}_h + \mathbf{F}_t = 0. \quad (14)$$

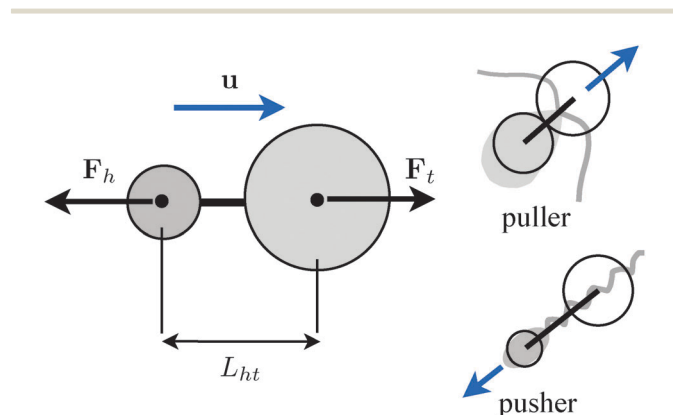


Fig. 6 Self-propelled asymmetric dumbbell model of a microswimmer with a flagellar tail.

The three equations above can be solved for  $\mathbf{F}_h$ ,  $\mathbf{F}_t$  and  $\mathbf{F}_p$ , given the frictional characteristics ( $\zeta_h$ ,  $\zeta_t$  and  $\boldsymbol{\Omega}$ ) and the velocity  $\mathbf{u}$ . Assuming that all forces and the velocity are directed along the axis of the dumbbell, if  $\mathbf{F}_h$ ,  $\mathbf{F}_t$  and  $\mathbf{F}_p$ , and  $\mathbf{u}$  are the axial force and velocity components, we obtain,

$$\mathbf{F}_t = -\mathbf{F}_h = \frac{\zeta_h}{1 - \boldsymbol{\Omega} \zeta_h} \mathbf{u}, \quad (15)$$

where  $\boldsymbol{\Omega} = 1/(4\pi\eta_s L_p)$  for Oseen–Burgers hydrodynamic interaction, and  $L_p$  is the distance between the head and tail centres. The magnitude of propulsive dipole is then

$$|\sigma| = |\mathbf{F}_h| L_p = \frac{12(\pi/2)\eta_s L_p^2 |\mathbf{u}|}{(L_p/a_h) - (3/2)}. \quad (16)$$

With  $\alpha$  defined as before i.e.  $|\sigma| = (\pi/2)\alpha\eta_s L^2 |\mathbf{u}|$  where  $L$  is the total end-to-end length of the swimmer, we obtain

$$\alpha = \frac{12(L_p/L)^2}{(L_p/a_h) - (3/2)}. \quad (17)$$

## Acknowledgements

The authors thank Sharadwata Pan (IITB-Monash Research Academy, Mumbai, India), David Hill (University of Melbourne, Australia) and Michael K. Danquah (Curtin University, Sarawak, Malaysia) for training AGM in microbiological techniques for culturing and preparing live/dead-cell suspensions of *E. coli* and *D. tertiolecta*.

## References

- 1 D. Chen, A. Lau, L. Hough, M. Islam, M. Goulian, T. Lubensky and A. Yodh, *Phys. Rev. Lett.*, 2007, **99**, 148302.
- 2 S. Ramaswamy, *Annu. Rev. Condens. Matter Phys.*, 2010, **1**, 323–345.
- 3 M. C. Marchetti, J. Joanny, S. Ramaswamy, T. B. Liverpool, J. Prost, M. Rao and R. A. Simha, *Rev. Mod. Phys.*, 2013, **85**, 1143–1189.
- 4 K. Drescher, J. Dunkel, L. H. Cisneros, S. Ganguly and R. E. Goldstein, *Proc. Natl. Acad. Sci. U. S. A.*, 2011, **108**, 10940–10945.
- 5 Y. Hatwalne, S. Ramaswamy, M. Rao and R. Simha, *Phys. Rev. Lett.*, 2004, **92**, 118101.
- 6 B. Haines, A. Sokolov, I. Aranson, L. Berlyand and D. Karpeev, *Phys. Rev. E: Stat., Nonlinear, Soft Matter Phys.*, 2009, **80**, 041922.
- 7 D. Saintillan, *Phys. Rev. E: Stat., Nonlinear, Soft Matter Phys.*, 2010, **81**, 056307.
- 8 D. Saintillan, *Exp. Mech.*, 2010, **50**, 1275–1281.
- 9 D. Saintillan and M. J. Shelley, *C. R. Phys.*, 2013, **14**, 497–517.
- 10 A. Sokolov and I. Aranson, *Phys. Rev. Lett.*, 2009, **103**, 148101.
- 11 J. Gachelin, G. Miño, H. Berthet, A. Lindner, A. Rousselet and E. Clement, *Phys. Rev. Lett.*, 2013, **110**, 268103.
- 12 R. Karmakar, R. Gulvady, M. S. Tirumkudulu and K. V. Venkatesh, *Phys. Fluids*, 2014, **26**, 071905.

- 13 S. Rafai, L. Jibuti and P. Peyla, *Phys. Rev. Lett.*, 2010, **104**, 098102.
- 14 E. A. Gaffney, H. Gadêlha, D. J. Smith, J. R. Blake and J. C. Kirkman-Brown, *Annu. Rev. Fluid Mech.*, 2011, **43**, 501–528.
- 15 P. K. Bhattacharjee, A. G. McDonnell, R. Prabhakar, L. Y. Yeo and J. R. Friend, *New J. Phys.*, 2011, **13**, 023005.
- 16 R. R. L. Guillard and J. H. Ryther, *Can. J. Microbiol.*, 1962, **8**, 229–239.
- 17 G. M. Gibbs, G. Orta, T. Reddy, A. J. Koppers, P. Martínez-López, J. L. de la Vega-Beltrán, J. C. Lo, N. Veldhuis, D. Jamsai, P. McIntyre, A. Darszon and M. K. O'Bryan, *Proc. Natl. Acad. Sci. U. S. A.*, 2011, **108**, 7034–7039.
- 18 G. McKinley and T. Sridhar, *Annu. Rev. Fluid Mech.*, 2002, **34**, 375–415.
- 19 P. Szabo, *Rheol. Acta*, 1997, **36**, 277–284.
- 20 G. McKinley and A. Tripathi, *J. Rheol.*, 2000, **44**, 653–670.
- 21 V. Entov and E. Hinch, *J. Non-Newtonian Fluid Mech.*, 1997, **72**, 31–53.
- 22 A. U. Chen, P. K. Notz and O. A. Basaran, *Phys. Rev. Lett.*, 2002, **88**, 174501.
- 23 D. C. Vadillo, T. R. Tuladhar, A. C. Mulji, S. Jung, S. D. Hoath and M. R. Mackley, *J. Rheol.*, 2010, **54**, 261–282.
- 24 D. C. Vadillo, W. Mathues and C. Clasen, *Rheol. Acta*, 2012, **51**, 755–769.
- 25 L. Campo-Deano and C. Clasen, *J. Non-Newtonian Fluid Mech.*, 2010, **165**, 1688–1699.
- 26 J. Arratia, P. E. Gollub and D. Durian, *Phys. Rev. E: Stat., Nonlinear, Soft Matter Phys.*, 2008, **77**, 36309.
- 27 W. C. Nelson, H. P. Kavehpour and C.-J. Kim, *Lab Chip*, 2011, **11**, 2424–2431.
- 28 J. Eggers and T. F. Dupont, *J. Fluid Mech.*, 1994, **262**, 205–221.
- 29 S. D. Ryan, B. M. Haines, L. Berlyand, F. Ziebert and I. S. Aranson, *Phys. Rev. E: Stat., Nonlinear, Soft Matter Phys.*, 2011, **83**, 050904.
- 30 I. M. Krieger and T. Dougherty, *J. Rheol.*, 1959, **3**, 137–152.
- 31 R. C. Ball and P. Richmond, *Phys. Chem. Liq.*, 1980, **9**, 99–116.
- 32 R. G. Larson, *The Structure and Rheology of Complex Fluids*, Oxford University Press, Oxford, 1999.
- 33 A. M. Wierenga and A. P. Philipse, *Colloids Surf., A*, 1998, **137**, 355–372.
- 34 B. H. Tan, K. C. Tam, Y. C. Lam and C. B. Tan, *J. Rheol.*, 2004, **48**, 915–926.
- 35 E. Hinch and L. Leal, *J. Fluid Mech.*, 1976, **76**, 187–208.
- 36 G. K. Batchelor, *J. Fluid Mech.*, 1970, **44**, 419–440.
- 37 B. ten Hagen, S. van Teeffelen and H. Löwen, *J. Phys.: Condens. Matter*, 2011, **23**, 194119.
- 38 J. Saragosti, P. Silberzan and A. Buguin, *PLoS One*, 2012, **7**, e35412.
- 39 S. T. Mortimer, *Hum. Reprod. Update*, 1997, 403–409.
- 40 H. Qi, M. M. Moran and B. Navarro, *Proc. Natl. Acad. Sci. U. S. A.*, 2007, **104**, 1219–1223.
- 41 S. D. Olson, S. S. Suarez and L. J. Fauci, *J. Theor. Biol.*, 2011, **283**, 203–216.
- 42 M. Doi and S. F. Edwards, *The Theory of Polymer Dynamics*, Oxford University Press, 1986.
- 43 J. Dunstan, G. Miño, E. Clement and R. Soto, *Phys. Fluids*, 2012, **24**, 011901.
- 44 P. V. Bayly, B. L. Lewis, E. C. Ranz, R. J. Okamoto, R. B. Pless and S. K. Dutcher, *Biophys. J.*, 2011, **100**, 2716–2725.
- 45 K. A. Schmitz, D. L. Holcomb-Wygle, D. J. Oberski and C. B. Lindemann, *Biophys. J.*, 2000, **79**, 468–478.
- 46 G. Subramanian and D. L. Koch, *J. Fluid Mech.*, 2009, **632**, 359–400.
- 47 A. A. Pahlavan and D. Saintillan, *Phys. Fluids*, 2011, **23**, 011901.
- 48 R. B. Bird, C. F. Curtiss, R. C. Armstrong and O. Hassager, *Dynamics of Polymeric Liquids*, Wiley-Interscience, New York, 2nd edn, 1987, vol. 2, Kinetic theory.